

Article

Design and Device Numerical Analysis of Lead-Free Cs₂AgBiBr₆ Double Perovskite Solar Cell

Tarek I. Alanazi 

Department of Physics, College of Science, Northern Border University, Arar 73222, Saudi Arabia; tarek.alanazi@nbu.edu.sa

Abstract: The advancement of lead-free double perovskite materials has drawn great interest thanks to their reduced toxicity, and superior stability. In this regard, Cs₂AgBiBr₆ perovskites have appeared as prospective materials for photovoltaic (PV) applications. In this work, we present design and numerical simulations, using SCAPS-1D device simulator, of Cs₂AgBiBr₆-based double perovskite solar cell (PSC). The initial calibrated cell is based on an experimental study in which the Cs₂AgBiBr₆ layer has the lowest bandgap ($E_g = 1.64$ eV) using hydrogenation treatment reported to date. The initial cell (whose structure is ITO/SnO₂/Cs₂AgBiBr₆/Spiro-OMeTAD/Au) achieved a record efficiency of 6.58%. The various parameters that significantly affect cell performance are determined and thoroughly analyzed. It was found that the conduction band offset between the electron transport layer (ETL) and the Cs₂AgBiBr₆ layer is the most critical factor that affects the power conversion efficiency (PCE), in addition to the thickness of the absorber film. Upon engineering these important technological parameters, by proposing a double ETL SnO₂/ZnO_{1-x}S_x structure with tuned absorber thickness, the PCE can be boosted to 14.23%.

Keywords: Cs₂AgBiBr₆; lead-free; double perovskite; double ETL; HTL; SCAPS-1D



Citation: Alanazi, T.I. Design and Device Numerical Analysis of Lead-Free Cs₂AgBiBr₆ Double Perovskite Solar Cell. *Crystals* **2023**, *13*, 267. <https://doi.org/10.3390/cryst13020267>

Academic Editors: Jing Wei and Fangze Liu

Received: 18 January 2023

Revised: 29 January 2023

Accepted: 31 January 2023

Published: 3 February 2023



Copyright: © 2023 by the author. Licensee MDPI, Basel, Switzerland. This article is an open access article distributed under the terms and conditions of the Creative Commons Attribution (CC BY) license (<https://creativecommons.org/licenses/by/4.0/>).

1. Introduction

Recently, a wide variety of photovoltaic (PV) technologies have been established by utilizing a vast number of photoactive absorber materials. Silicon solar cells are the most widely used cells as they share over 90% of the global solar market [1], while their efficiencies have reached more than 26% [2]. Because of their relatively high cost, various efforts were dedicated to producing high-efficiency low-cost Si-based solar cells [3–6]. Similar p-n homojunction structures were investigated [7–10]; however, more studies are needed to improve the reported efficiencies. Other heterojunction-based alternatives have also attracted great interest, such as thin-film solar cells, especially perovskite p-i-n heterojunction solar cells, in both research and industrial fields. Essentially, perovskite solar cells (PSCs) are believed to be the most promising next-generation PV technologies [11].

After enormous attempts in the optimization of materials and devices, PSCs have achieved record efficiencies of more than 25% [12]. Usually, higher efficiencies are obtained from lead-based PSCs [13–15]. However, lead-based cells face some issues, such as declined performance upon subjecting to moisture and light [16,17], in addition to toxicity, which is considered a major obstacle to the commercialization of such cells [18]. To conquer the current deficiency associated with the existence of lead in PSCs, some other additives, with the same lead group, were extensively researched. These include, for instance, tin [19,20] and germanium [21]. However, tin-based PSCs have another chief disadvantage corresponding to the oxidation of Sn²⁺ to Sn⁴⁺ resulting in instability issues [22]. Other alternative ways have also been investigated. These include replacing the Pb²⁺ ion with one monovalent combined with one trivalent ion such as Cs₂AgBiBr₆ [23], Cs₂AgBiCl₆ [24], and (CH₃NH₃)₂AgBiBr₆ [25] double perovskite configurations. Of these candidates, Cs₂AgBiBr₆, in which the lead is replaced by silver (Ag⁺) combined with

bismuth (Bi^{3+}) cations, has been reported as the most promising structure thanks to its high crystallinity, long carrier lifetime, and good stability compared to the lead-based perovskite [26].

Numerous experimental efforts have been performed to improve the properties of $\text{Cs}_2\text{AgBiBr}_6$ PSC, thereby increasing the PCE of the produced solar cell. In [27], a PCE of about 2.5% was obtained for an experimental configuration of FTO/ TiO_2 / $\text{Cs}_2\text{AgBiBr}_6$ /Spiro-OMeTAD/Au. Another study reveals a PCE of 2.23% in an inverted planar heterojunction architecture [28]. Further, C. Wu et al. fabricated a structure of ITO/ SnO_2 / $\text{Cs}_2\text{AgBiBr}_6$ / P_3HT /Au, and the resulting PCE was 1.44% [29]. In addition to the efforts made in improving the quality of the $\text{Cs}_2\text{AgBiBr}_6$ absorber, some studies were devoted to investigating alternative electron transport layers (ETLs) reporting enhanced efficiencies of up to 4.23% [30]. As can be observed from these studies, the reported PCEs of double perovskite $\text{Cs}_2\text{AgBiBr}_6$ -based solar cells are still much lower than those achieved by traditional lead-based PSCs despite their superior stability. This can be attributed to its wide bandgap, which exceeds 2 eV, which limits its light absorption capability. Additionally, the high defects encountered in $\text{Cs}_2\text{AgBiBr}_6$ films result in low carrier lifetimes in the range of 13.7 ns [31]. Recently, by using a hydrogenation technique, the bandgap and carrier lifetime of $\text{Cs}_2\text{AgBiBr}_6$ films have been engineered from 2.18 eV down to 1.64 eV and from 18.85 ns up to 41.86 ns, respectively, resulting in a champion efficiency of 6.37% [32].

To facilitate more efficient studies, design recommendations for the solar cell should be highlighted and are extremely needed. In this context, SCAPS-1D device simulator has been extensively used in the simulation and design of thin-film solar cells [33–37]. Concerning previous simulation efforts related to $\text{Cs}_2\text{AgBiBr}_6$, two designed cells were compared with two different HTLs, namely organic P_3HT and inorganic Cu_2O . The calculated optimized efficiencies, using SCAPS simulator, for P_3HT -based and Cu_2O -based cells were 11.69% and 11.32%, respectively [38]. Recently, a device structure of FTO/ ZnO / $\text{Cs}_2\text{AgBiBr}_6$ / NiO /Au has been proposed [39]. It was found that, by using SCAPS simulator, the PCE declines from 21.88% to 1.58% as the minority carrier lifetime reduces from 1 μs to 0.1 ns [39].

Accordingly, in this simulation work, the key factors restricting the performance enhancement of the $\text{Cs}_2\text{AgBiBr}_6$ -based PSCs are thoroughly investigated. These factors include the bandgap energy and carrier lifetime of the absorber as well as the proper choices of the ETL and HTL materials to achieve an optimum band alignment. First, the study is initiated by selecting a recent hydrogenated $\text{Cs}_2\text{AgBiBr}_6$ solar cell that was fabricated based on the structure ITO/ SnO_2 / $\text{Cs}_2\text{AgBiBr}_6$ /Spiro-OMeTAD/Au [32]. Based on the calibration of the simulated vs experimental cell behavior, the validation of the physical models and distinct parameters is proved. Further, the design of the initial cell is carried out in consecutive steps. It is found that the most severe issue causing the degradation of the cell is the inappropriate value of the conduction band offset (CBO) between the SnO_2 ETL and $\text{Cs}_2\text{AgBiBr}_6$. Therefore, the design of CBO is performed by proposing a double ETL structure. Next, the main material properties of $\text{Cs}_2\text{AgBiBr}_6$ to understand their impact on the performance of the cell and to determine the most effective parameters which are responsible for the performance enhancement. This study is the first to be implemented, to the best of our knowledge, on a $\text{Cs}_2\text{AgBiBr}_6$ -based PSC with the lowest recorded bandgap ($E_g = 1.64$ eV) and highest PCE to date. All simulations are performed under AM1.5G illumination utilizing SCAPS-1D device simulator.

2. Simulation Method and Device Structure and Materials

2.1. SCAPS Simulation Method

SCAPS simulator was created at ELIS, University of Gent [40]. In SCAPS software, up to seven semiconductor layers can be implemented. It is a very efficient and widely used device simulator software that is employed to handle a lot of different solar cell structures, thin film solar cells, in particular, with a massive variety of materials [41–48]. This device simulator is capable of analyzing various solar cells' output indicators of the solar cell under investigation, such as J - V characteristics, ac characteristics in terms of capacitance

(C-V and C-f), and spectral response in terms of external quantum efficiency (EQE). The main PV factors can be attained easily through the J - V curve. Those include V_{OC} , J_{SC} , FF, and PCE. Moreover, physical behavior trends can be traced via energy band diagrams, carrier concentration, electric field, recombination rates, and others in the different regions of the cell. The simulator solves the semiconductor basic equations iteratively to get the desired output according to the input parameters by the user [49].

SCAPS simulator solves the one-dimensional Poisson's equation along with continuity equations using a numerical technique. Poisson's equation is given in Equation (1), while the continuity equations of charge carriers (electrons and holes) are provided in Equations (2) and (3). Additionally, the simulation package solves the drift-diffusion model to get the transport parameters of the electrons and holes. Based on this model, the corresponding electron and hole current densities (J_n and J_p) are calculated as in Equations (4) and (5).

$$\frac{d^2\psi}{dx^2} = \frac{q}{\epsilon} (n - p + N_A^- - N_D^+ + n_t - p_t) \quad (1)$$

$$\frac{1}{q} \frac{dJ_n}{dx} = R_n - G(x) \quad (2)$$

$$\frac{1}{q} \frac{dJ_p}{dx} = G(x) - R_p \quad (3)$$

$$J_n = -\frac{n\mu_n}{q} \frac{dE_{Fn}}{dx} \quad (4)$$

$$J_p = +\frac{p\mu_p}{q} \frac{dE_{Fp}}{dx} \quad (5)$$

The trapped densities are denoted by n_t and p_t , while n , and p denote the electron and hole concentrations, respectively. The doping levels of ionized acceptors and donors are termed N_A^- and N_D^+ , respectively. ψ is the potential across the device, q is the electron charge, and ϵ is the permittivity. The mobility and quasi-Fermi level are expressed by μ and E_F , respectively. The generation rate $G(x)$ is given in Equation (6), where x is the distance computed below the illuminated surface,

$$G(x) = \int_0^\infty G(\lambda, x) d\lambda = \int_{\lambda_1}^{\lambda_2} \alpha(\lambda)(1 - r(\lambda))N(\lambda, 0)Q(\lambda)e^{-\alpha(\lambda)x} d\lambda \quad (6)$$

Here, $\alpha(\lambda)$ and $r(\lambda)$ are the absorption and reflection coefficients, respectively, while $Q(\lambda)$ and $N(\lambda, 0)$ are the internal quantum efficiency and incident photon flux (in Photons/s·m²), respectively.

Moreover, the calculated recombination rates of electrons and holes include radiative and deep traps. The recombination through deep traps is evaluated through the Shockley Read Hall (SRH) recombination mechanism. In bulk, the rate due to SRH model is provided in Equation (7). The model is characterized by a minority carrier lifetime (τ), which depends on the defect density (N_t) as given in Equation (8). The interfacial recombination rates are computed by the Pauwels-Vanhoutte model [50].

$$R_{SRH} = \frac{(np - n_i^2)}{\tau \left(p + n + 2n_i \cosh \left(\frac{E_t - E_i}{k_B T} \right) \right)} \quad (7)$$

$$\tau = \frac{1}{\sigma N_t v_{th}} \quad (8)$$

where σ is the capture cross-section (either for electrons or holes) and v_{th} is the thermal speed, while E_t is the trap energy level position and E_i is the intrinsic level.

2.2. Solar Cell Structure and Materials

Figure 1a illustrates the main device structure. The device configuration is based on ITO/SnO₂/Cs₂AgBiBr₆/Spiro-OMeTAD/Au as indicated where SnO₂ and Spiro-OMeTAD serve as ETL and HTL, respectively [32]. The thicknesses of the materials as well as the main absorber characteristics are taken from an experimental work [32]. The band alignment before contact, displayed in Figure 1b, denotes the electron affinities and energy bandgaps of the various layers. The values of corresponding energy levels are obtained from the literature [32,38]. Upon subjecting the cell to AM1.5G light illumination, electron-hole pairs are generated. Then, the electrons are transformed in such a way as to migrate toward the front ITO contact while being blocked by the HTL. On the other hand, the generated holes are directed toward the back Au contact while being blocked by the ETL as illustrated in Figure 1b. Moreover, the lattice structure is displayed in Figure 1c for a single Cs₂AgBiBr₆ crystal showing a well-crystalline and phase-pure octahedral structure as revealed in REF [51].

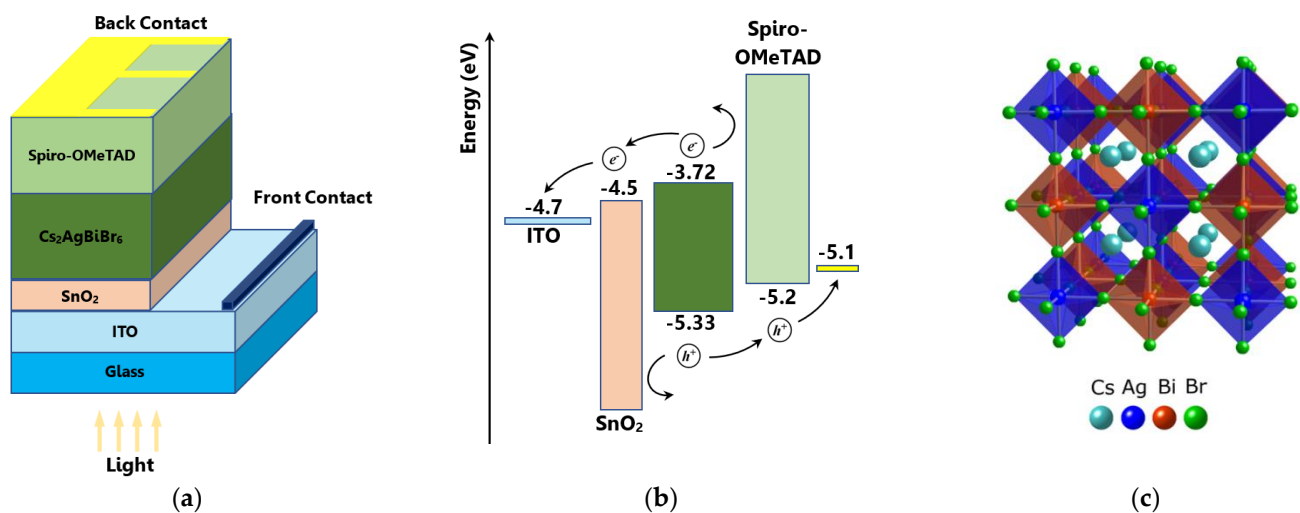


Figure 1. (a) Device structure of ITO/SnO₂/Cs₂AgBiBr₆/Spiro-OMeTAD/Au and (b) band alignment before contact, and (c) lattice structure of a single Cs₂AgBiBr₆ crystal (Reprinted with permission from [51]. Copyright 2018, American Chemical Society).

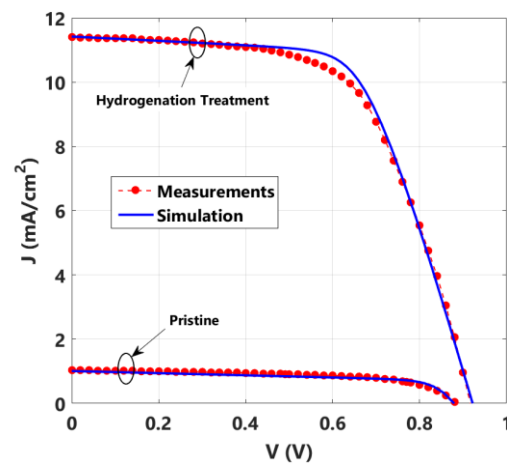
The bulk defect density for Cs₂AgBiBr₆ is taken to be in the order of $1 \times 10^{16} \text{ cm}^{-3}$ as measured for this absorber [52]. A single energetic distribution having a defect level at 0.8 eV is taken as a deep defect. The electron and hole capture cross-sections in the bulk were calculated to be approximately $2 \times 10^{-16} \text{ cm}^2$ to obtain a carrier lifetime of a little above 40 ns as measured in [32]. Moreover, the carrier mobility was taken as the measured value at $9.28 \text{ cm}^2 \text{ V}^{-1} \text{ s}^{-1}$ [32]. At both interfaces, the electron and hole capture cross-sections are kept at 10^{-15} cm^2 where the capture cross-sections of both electrons and holes are taken to be equal, while the interfacial defect density at both SnO₂/Cs₂AgBiBr₆ and Cs₂AgBiBr₆/Spiro-OMeTAD interfaces is taken to be $1 \times 10^{10} \text{ cm}^{-2}$, resulting in a carrier surface recombination velocity of 10^2 cm/s . Also, the thermal velocity of electrons and holes is the same ($v_{th} = 1 \times 10^7 \text{ cm/s}$). The previous material parameters along with other parameters such as relative permittivity, conduction and valence DOSs, as well as doping concentrations, are also indicated in Table 1.

Table 1. Primary input material parameters of the solar cell [32,38,39,46].

Parameters	ITO	SnO ₂	Cs ₂ AgBiBr ₆	Spiro-OMeTAD	Au
<i>t</i> (nm)	100	40	140	300	50
Electron affinity (eV)		4.40	3.72	2.20	
Bandgap energy (eV)		3.50	1.64	3.00	
Relative permittivity		9.0	5.8	3.0	
Electron mobility (cm ² /V·s)		240	9.28	2 × 10 ⁻⁴	
Hole mobility (cm ² /V·s)		25	9.28	2 × 10 ⁻⁶	
Effective conduction DOS (cm ⁻³)		2.2 × 10 ¹⁸	1 × 10 ¹⁶	2.2 × 10 ¹⁸	
Effective valence DOS (cm ⁻³)		1.8 × 10 ¹⁹	1 × 10 ¹⁶	1.8 × 10 ¹⁹	
Donor density (cm ⁻³)		2 × 10 ¹⁹	-	-	
Acceptor density (cm ⁻³)		-	1 × 10 ¹⁴	1 × 10 ¹⁹	
Work function (eV)	4.7	-	-	-	5.1

2.3. SCAPS Calibration

In this subsection, the physical models and material parameters presented in the previous subsections are implemented to simulate the initial cell subjected to the same conditions as encountered in the experimental study in REF [32]. The *J-V* curves of the experimental and simulated cells are provided in Figure 2 while a comparison between the SCAPS results and those from measurements is provided in Table 2. The target hydrogenated cell whose bandgap is 1.64 eV is also compared to the pristine cell whose bandgap is 2.18 eV. When considering the pristine cell without hydrogenation, the carrier mobility is 1.71 cm²V⁻¹s⁻¹, and the carrier lifetime is only 18.85 ns [32]. As indicated in Figure 2, the performance of the pristine cell is much lower than that of the hydrogenated cell due to the differences in bandgap, mobility, and lifetime. The decent agreement between measurements and SCAPS results reveals the appropriate calibration of the tool.

**Figure 2.** *J-V* characteristics of hydrogenated and pristine cells for measurements vs. SCAPS simulations.**Table 2.** Comparison between PV cell metrics for measured and simulated hydrogenated cells.

	<i>V</i> _{OC} [V]	<i>J</i> _{SC} [mA/cm ²]	FF [%]	PCE [%]
Measurements [32]	0.920	11.40	60.93	6.37
SCAPS Simulation	0.921	11.41	63.10	6.64

3. Results and Discussion

In this section, the influence of the key cell parameters is examined to provide some design guidelines to improve the PCE of the calibrated solar cell. First, a physical analysis

is performed to investigate the most crucial parameters that limit the performance of the initial cell. One of the key factors is the band alignment between the different interfaces. This can be indicated by the CBO and VBO between the ETL/absorber and absorber/HTL interfaces that significantly affect cell performance. In addition, the thickness and carrier lifetime of the photoactive absorber come as crucial parameters to be studied. Additionally, in each step of investigation regarding each parameter we explore, the influence on the figures of merit PV parameters is given and compared. A physical explanation of the various trends is likewise given in each step.

3.1. Determination of Critical Design Parameters

First, to highlight the underlying physics of the behavior of the initial cell, the different simulated current components are plotted as displayed in Figure 3a. This step is important to determine the most critical parameters that need to be engineered in order to alleviate the issues related to the operation of the cell under study. The figure shows the total generation and recombination currents which are equal at V_{OC} . The minority currents at the back and front contacts are also shown. More importantly, the bulk and interface current components are demonstrated. The trend of these currents indicates that the interface recombination is higher than the bulk one. The higher interface recombination is not desirable as it causes cell degradation. This result can be further assessed by plotting the energy band diagram as shown in Figure 3b.

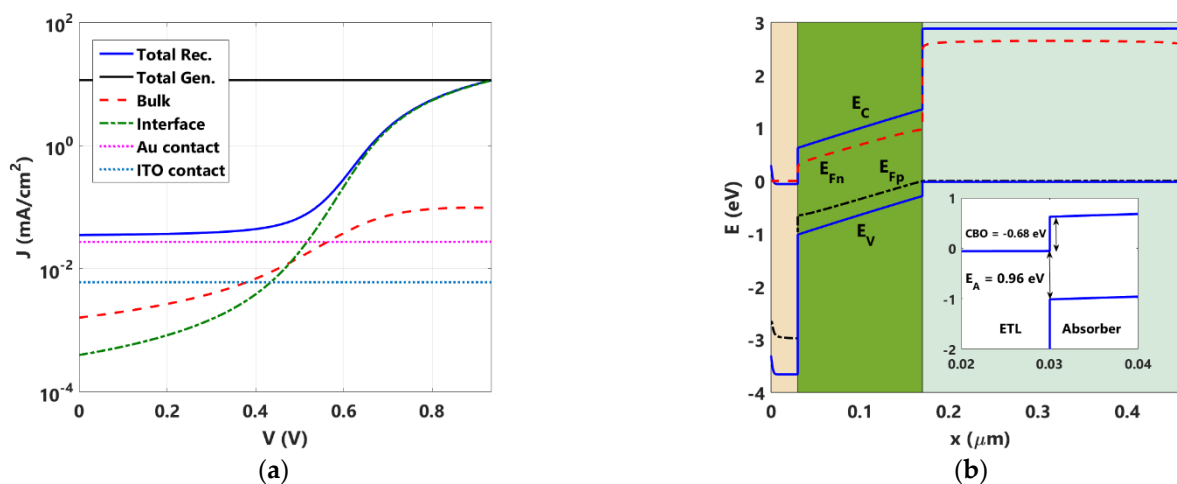


Figure 3. (a) Current components and (b) energy band diagram at short-circuit and illuminated conditions (showing band offset in the inset) of the initial calibrated cell.

Eventually, higher PCEs are achieved in type-I ETL/absorber interface that is characterized by a spike-type junction in which the CBO is positive [53]. Notably, the CBO is calculated as the difference between the electron affinities at the absorber and ETL sides (i.e., $CBO = \chi_{\text{absorber}} - \chi_{\text{ETL}}$). For small positive values of the CBO, the charge carriers flow is appropriate, resulting in a prevalent recombination mechanism in the bulk (absorber), which is desirable [54]. However, if the CBO is high enough, a barrier will be formed, causing a hurdle to the electron transport. On the other hand, when the CBO is negative, a cliff-type junction occurs, which does not prevent electron transport; however, the activation energy (E_A) is lower than the absorber bandgap, resulting in increased interface recombination compared to the bulk recombination, causing a degraded functioning [54,55]. The previous discussion is, however, valid for the single ETL design.

Now, referring to Figure 3b, it is obvious that the $\text{SnO}_2/\text{Cs}_2\text{AgBiBr}_6$ interface is of a cliff style as the CBO is -0.68 eV. The activation energy is also indicated in the inset of the figure, which has a value of 0.96 eV. The results clearly reveal the inappropriate design of this CBO. On the other hand, it is depicted in Figure 3b that the band alignment is suitable for the $\text{Cs}_2\text{AgBiBr}_6/\text{Spiro-OMeTAD}$ interface as electron blocking is satisfied. In addition,

the hole transport from the $\text{Cs}_2\text{AgBiBr}_6$ active layer to the HTL is facilitated via the small offset. Based on these results, one can conclude that the main issue in the initial cell comes from the improper alignment manifested from the CBO, while the VBO has no issue. It should be pointed out here that the alignment of SnO_2 with the ITO contact is suitable as the majority carrier barrier height is about 0.357 eV, which, to a high extent, does not affect the hole injection into the contact.

3.2. Proposed Double ETL Structure

Notably, promoting charge collection and separation is considered one of the most favorable strategies to enhance the overall performance of a solar cell. As discussed herein, the ETL plays an important role in this regard. Actually, some experimental studies have been conducted to develop double ETL by using two materials instead of only using a single ETL to overcome the issues discussed in the previous subsection. For instance, the influence of double TiO_2 /PFN ETL on the performance of organic P3HT:PC₆₁BM-based solar cells was investigated and it was found that the PCE increases up to 2.5 times compared to that of single ETL cells [56]. Further, a double TiO_2 / SnO_2 ETL was employed resulting in a PCE improvement from 18.02% to 21.13% for a lead-based PSC [57]. Double Nb_2O_5 / ZnO ETL was also applied in lead-based PSCs, resulting in a high device performance in terms of efficiency and stability thanks to the energy band matching between the ETLs and the absorber and the ITO contact [58]. Thus, development of double ETL (DETL) is, remarkably, an encouraging approach to accomplish both band alignment at the ITO and absorber interfaces. Essentially, using DETL, the benefits of various ETL materials can be realized while avoiding their drawbacks. Thus, we proceed our study by investigating another ETL material along with SnO_2 to form a DETL (SnO_2 is used in contact to the ITO because it has a good alignment). The aim of this design is to facilitate and offer some possible solutions that can be utilized to achieve the proper band alignment throughout the whole proposed lead-free PSC.

A suitable candidate that can be combined with SnO_2 to form a double ETL is the ternary compound $\text{Zn}(\text{O}, \text{S})$, which has a lot of advantages that include its bandgap and affinity tunability as well as its high mobility. It has been experimentally realized in a double $\text{Zn}(\text{O}, \text{S})/\text{CdS}$ ETL and showed promising results [59]. The energy gap and the electron affinity of $\text{ZnO}_{1-x}\text{S}_x$ vary from 3.30 eV to 3.76 eV and from 4.50 eV to 3.14 eV, respectively, upon increasing the sulfur composition (x) from zero to one. Other electrical and optical parameters for $\text{ZnO}_{1-x}\text{S}_x$ are obtained from the literature to continue the simulation [59,60]. The change in the electron affinity and the energy gap against x is illustrated in Figure 4a [59,60]. Moreover, the CBO between $\text{ZnO}_{1-x}\text{S}_x$ and $\text{Cs}_2\text{AgBiBr}_6$ is shown.

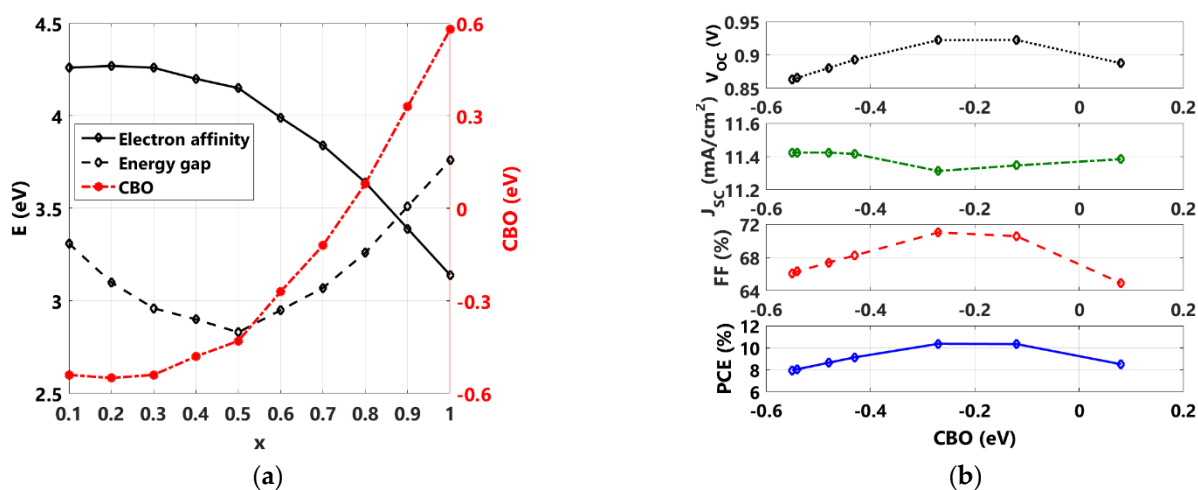


Figure 4. (a) Change in electron affinity and energy gap of the $\text{ZnO}_{1-x}\text{S}_x$ (x is sulfur composition). The CBO at $\text{ZnO}_{1-x}\text{S}_x/\text{Cs}_2\text{AgBiBr}_6$ interface is also plotted and (b) variation of PV parameters with respect to CBO.

It should be noted here that the design of the double ETL is different from that of the single ETL as there are other contradicting effects aside from the CBO. That is why the sweep of the CBO is to be expanded in the next simulation to widen the analysis. The simulation results in terms of the PV parameters variation with the CBO is pictured in Figure 4b. In this simulation, the range of the CBO is taken from -0.55 eV to $+0.08$ eV, as the performance deteriorates beyond this value. These values correspond to a sulfur composition from 0.2 to 0.8. As the CBO increases, both V_{OC} and FF increase as well while J_{SC} decreases slowly. After a certain value of CBO, both V_{OC} and FF decrease but J_{SC} is almost unchanged. The overall effect on the PCE is that it increases and then decreases. There is a flat region from $CBO = -0.27$ up to -0.12 eV; however, a maximum PCE of 10.35% is observed at a CBO of -0.27 eV, which is not expected as it is characterized by a low spike-like interface. However, again, this proposed design is not the same as the single ETL, and that is why it gives a different trend. This value of CBO can be attained for a sulfur composition of 0.6, i.e., for $ZnO_{0.4}S_{0.6}$ compound.

The previous results can be assessed by drawing the J - V characteristics as shown in Figure 5 where four cases are shown in the figure. The first case is regarding the initial cell with a single SnO_2 ETL. The other three cases represent the difference between various CBO values. For $CBO = +0.08$ eV, the compound used is $ZnO_{0.2}S_{0.8}$ (as $x = 0.8$), while for $CBO = -0.55$ eV, the compound used is $ZnO_{0.8}S_{0.2}$ (as $x = 0.2$). The final case is for the optimal PCE, which occurs when using $ZnO_{0.4}S_{0.6}$ (corresponding to $CBO = -0.27$ eV). Moreover, a physical explanation of the behavior of the cell upon applying the DETL design can be understood by drawing the energy band diagram for the three design cases. As clearly indicated in Figure 6, there are two competing band offsets that may influence the performance. Regarding Figure 6a, which illustrates the case of $SnO_2/ZnO_{0.2}S_{0.8}$, although the band alignment at $ZnO_{0.2}S_{0.8}/Cs_2AgBiBr_6$ is a suitable small spike band, the extremely high barrier at the $SnO_2/ZnO_{0.2}S_{0.8}$ interface is the main cause to limit the carrier flow. That is to say, the carriers are easily injected from the absorber but face an obstacle at the interface between the two ETLs. On the other hand, while the band offset at the $ZnO_{0.4}S_{0.6}/Cs_2AgBiBr_6$ interface is a cliff band (see Figure 6b), the barrier between the two ETLs becomes slower, and the carrier transport is enhanced. Finally, regarding Figure 6c, the cliff band becomes severe and, in turn, recombination will be very large. Although, in this case, the barrier between the two ETLs is the lowest amongst the three cases, the transport is minimal due to the cliff at the $ZnO_{0.8}S_{0.2}/Cs_2AgBiBr_6$ interface. This behavior is apparently reflected on the J - V curve given in Figure 5.

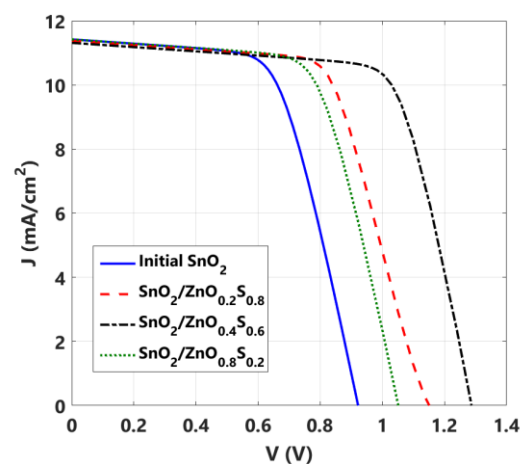


Figure 5. Comparison of illuminated J - V characteristics between different cases of design including initial cell with a single ETL and three different cases of double ETL.

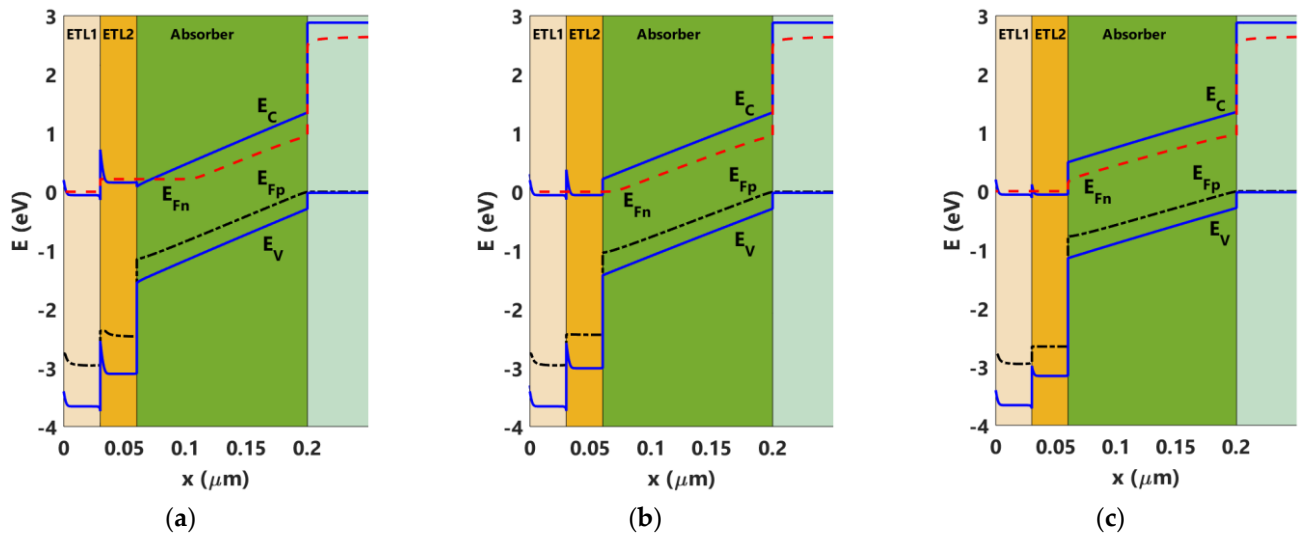


Figure 6. Energy band diagrams at short-circuit and illuminated conditions of three design cases of ternary compound $\text{ZnO}_{1-x}\text{S}_x$: (a) $\text{ZnO}_{0.2}\text{S}_{0.8}$, (b) $\text{ZnO}_{0.4}\text{S}_{0.6}$ and (c) $\text{ZnO}_{0.8}\text{S}_{0.2}$.

3.3. Absorber Parameters Optimization

The thickness of the photoactive film (t_{abs}) in a solar cell is a critical characteristic that can effectively regulate the function of the thin-film solar cell. In order to be able to increase the collection efficiency of the photogenerated carriers inside a solar cell, it is required to have a long diffusion length (L) for the minority carriers inside the absorber. The diffusion length is defined as in Equation (9):

$$L = \sqrt{\frac{kT}{q} \mu \tau} \quad (9)$$

If $L \ll t_{\text{abs}}$, the carriers may recombine before transferring to the contacts. On the other hand, if t_{abs} is very thin, then the probability of absorbing the incident photons will be limited because of the inadequate absorber thickness. Thus, there should be a careful design for the L and t_{abs} to enable higher photon absorption rates besides lower recombination rates following carrier collection. t_{abs} should be high enough but not higher than L . It can be deduced from Equation (8) that if the defect density is reduced, the carrier lifetime becomes higher, resulting in longer diffusion lengths. Therefore, an increase in defect density will be unfavorable to cell operation. Hence, for a proper design of the absorber material, it is important to simultaneously study the impact of thickness and defect density as they are closely related. In the next simulation, the absorber thickness and bulk defect density are concurrently varied.

The variation in the PCE against the absorber thickness and defect density (N_t) is exhibited in Figure 7 for two cases, namely the initial cell in which a single ETL is adopted (Figure 7a), while the second case is corresponding to the optimum case obtained from the double $\text{SnO}_2/\text{ZnO}_{0.4}\text{S}_{0.6}$ ETL design (Figure 7b). In this simulation, t_{abs} is varied in the range 100 nm to 520 nm while N_t is varied from 1×10^{13} to $1 \times 10^{17} \text{ cm}^{-3}$. It can be inferred from the figure, for both cases, that as the absorber becomes wider, the PCE progressively enhances thanks to the improvement in photon absorption. When the absorber thickness becomes higher than 300 nm (for the single ETL case) or 350 nm (for the DETL case), the PCE becomes almost unchanged. This is due to the fact that the thickness is now comparable to the diffusion length and any further increase in the thickness will result in more bulk recombination, which will deteriorate the performance. It is also noted that the impact of the defect density is minor in proportion to that of the absorber thickness. Therefore, to obtain an enhanced PCE, it is adequate to control the thickness while keeping

reasonable trap densities. Increasing the thickness beyond 300 nm can result in a PCE of higher than 8% or 14% in the case of the calibrated cell or the double ETL cell, respectively.

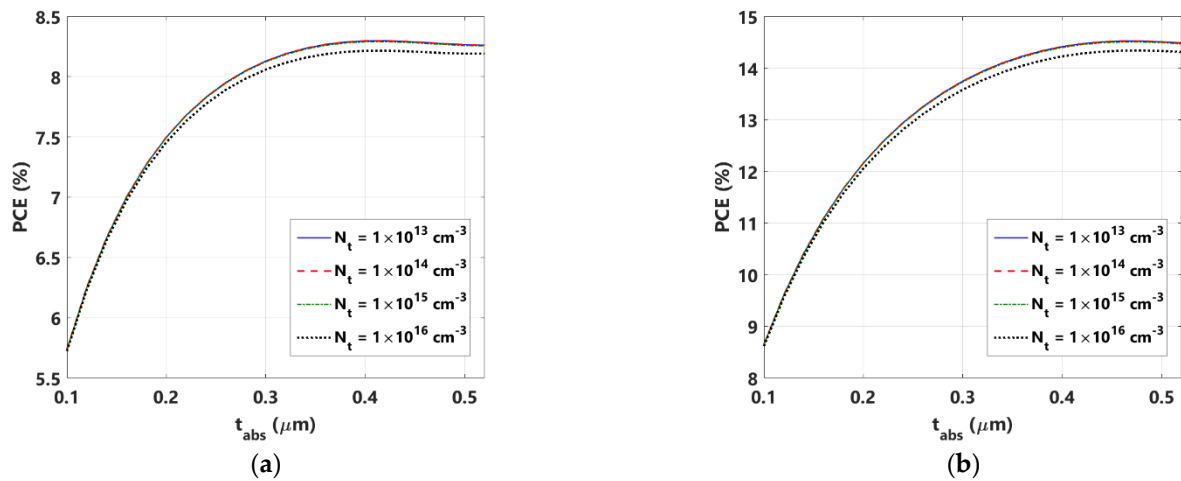


Figure 7. Impact of absorber thickness and bulk defect density on the efficiency of (a) initial cell and (b) double ETL cell.

3.4. Possible Indoor Applications

To investigate the possibility of the presented lead-free PSC for use in indoor applications where the light intensity is low, the initial cell and an optimized double ETL cell are simulated under low levels of intensity. When simulating the initial cell, all parameters indicated in Table 1 are applied. On the other hand, when simulating the double ETL cell, an optimized thickness of 400 nm is taken while keeping the same initial trap density. Figure 8 shows the results in terms of the PV parameters for the initial cell (Figure 8a) and optimized DETL cell (Figure 8b). It can be depicted in the trend of the cells that despite the decline in V_{OC} and J_{SC} , the FF is enhanced when the light intensity decreases until 40 mW/cm^2 . As the input power becomes lower for reduced intensities, the overall impact is that the PCE slightly boosts. For lower intensities below 40 mW/cm^2 , the PCE significantly decreases due to the dominant effect of both V_{OC} and J_{SC} . The presented results reveal the suitability of the designed cell to be utilized in indoor applications down to a certain low light intensity level.

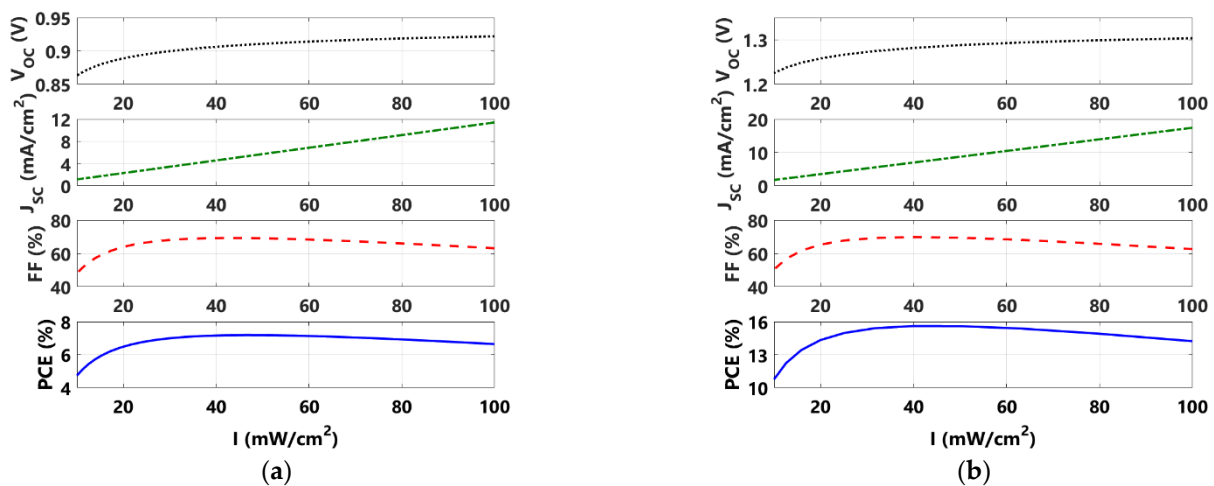


Figure 8. Influence of light intensity on the PV performance parameters of (a) initial cell and (b) optimized DETL cell.

Finally, to compare the initial cell and other designed DETL cells, the J - V characteristics are presented in Figure 9. Moreover, the figure shows the case when neglecting the effect of the series and shunt resistance to give a figure of merit of the efficiency promotion limit. The PCE of each case is highlighted in the figure. Additionally, Table 3 addresses the PV parameters of the design cases of DETL (with and without absorber optimization) besides the corresponding parameters of some state-of-the-art $\text{Cs}_2\text{AgBiBr}_6$ -based solar cell devices either from simulation or experimental research studies. The main absorber parameters are also indicated in the table. The table obviously demonstrates the crucial impact of the bandgap energy. Despite the higher values of the V_{OC} when E_g is high, the reported PCEs are lower than those reported for lower E_g mainly because of the low J_{SC} . Based on the current simulation, we believe that the combination of ETLs along with growing relatively thicker $\text{Cs}_2\text{AgBiBr}_6$ films would pave the way for obtaining high efficiency $\text{Cs}_2\text{AgBiBr}_6$ -based solar cells which are non-toxic and eco-friendly that can be suitable for many applications. To further boost the efficiency of $\text{Cs}_2\text{AgBiBr}_6$ -based devices, more experimental work should be carried out in order to improve the quality of the bulk and interfaces to minimize the defects and thus lower recombination losses. A high-quality absorber, low interfacial recombination velocities, and good contacts to reduce R_s are extremely needed to reach the theoretical efficiency which is about 29.5% on the ground of the ideal Shockley–Queisser limit, given a bandgap of 1.64 eV [61].

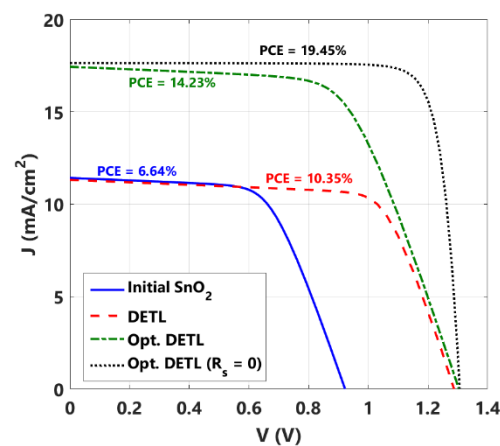


Figure 9. Illuminated J - V characteristics for single and double ETL including two optimization steps (for absorber thickness and series resistance).

Table 3. Comparison of various experimental and simulation studies.

Cell Structure (ETL/Absorber/HTL)	E_g (eV)	t_{abs} (nm)	τ (ns)	V_{OC} (V)	J_{SC} (mA/cm ²)	FF (%)	PCE (%)	Ref.
$\text{SnO}_2/\text{Cs}_2\text{AgBiBr}_6/\text{P}_3\text{HT}$	2.05	150	30	1.04	1.78	78.00	1.44	[29]
$\text{TiO}_2/\text{C-Chl}/\text{Cs}_2\text{AgBiBr}_6/\text{Spiro-OMeTAD}$	2.07	200	NA	1.04	4.09	73.12	3.11	[30]
$\text{SnO}_2/\text{Cs}_2\text{AgBiBr}_6/\text{Spiro-OMeTAD}$	1.64	140	41.86	0.92	11.40	60.93	6.37	[32]
$\text{SnO}_2/\text{Cs}_2\text{AgBiBr}_6/\text{P}_3\text{HT}$	2.05	1200	100	2.02	6.39	90.00	11.69	[38]
$\text{ZnO}/\text{Cs}_2\text{AgBiBr}_6/\text{NiO}$	1.70	700	1000	1.29	20.69	81.72	21.88	[39]
$\text{SnO}_2/\text{ZnOS}/\text{Cs}_2\text{AgBiBr}_6/\text{Spiro-OMeTAD}$	1.64	140	41.86	1.29	11.31	71.00	10.35	This work
$\text{SnO}_2/\text{ZnOS}/\text{Cs}_2\text{AgBiBr}_6/\text{Spiro-OMeTAD}$	1.64	400	41.86	1.30	17.44	62.59	14.23	This work

4. Conclusions

This simulation study analyzed a low bandgap $\text{Cs}_2\text{AgBiBr}_6$ -based PSC and provides some design recommendations for this type of cell. A cell arrangement of $\text{FTO}/\text{SnO}_2/\text{Cs}_2\text{AgBiBr}_6/\text{Spiro-OMeTAD}/\text{Au}$ has been adopted, which is based on a previous experimental work. After the calibration of the simulation versus available experimental data, the key factors that are responsible of limiting the efficiency were highlighted and

investigated. It was found that although the absorber/HTL and ITO/SnO₂ interfaces are well-designed due to the appropriate band alignment, the SnO₂/absorber interface was found to suffer from high recombination due to band misalignment. In order to resolve this issue while keeping other advantages intact, a double ETL structure has been proposed. An optimum structure was found to alleviate the absorber/ETL issue by incorporating ZnO_{0.4}S_{0.6}/Cs₂AgBiBr₆ DETL system. Moreover, the PCE before and after absorber optimization was found to be 10.35% and 14.23% for an absorber thickness of 140 nm and 400 nm for the single and double ETL structures, respectively. Moreover, the performance of the proposed cell was investigated in low light intensity conditions, and the results revealed that a better functioning of the cell may be obtained for just an intensity of 40 mW/cm² at which the PCE is 15.61% for the optimized DETL cell. Overall, the produced results imply that low bandgap Cs₂AgBiBr₆ can play a significant role as an absorber layer to achieve a highly efficient, eco-friendly, stable PSC technology for outdoor and indoor applications.

Funding: This research received no external funding.

Institutional Review Board Statement: Not applicable.

Informed Consent Statement: Not applicable.

Data Availability Statement: Not Applicable.

Acknowledgments: The author extends his appreciation to the Deanship of Scientific Research at Northern Border University for their support. The author is grateful to the Prince Faisal bin Khalid bin Sultan Research Chair in Renewable Energy Studies and Applications (PFCRE) at Northern Border University for their support and assistance.

Conflicts of Interest: The author declares no conflict of interest.

References

1. Okil, M.; Salem, M.S.; Abdolkader, T.M.; Shaker, A. From Crystalline to Low-cost Silicon-based Solar Cells: A Review. *Silicon* **2022**, *14*, 1895–1911. [CrossRef]
2. Yoshikawa, K.; Kawasaki, H.; Yoshida, W.; Irie, T.; Konishi, K.; Nakano, K.; Uto, T.; Adachi, D.; Kanematsu, M.; Uzu, H.; et al. Silicon heterojunction solar cell with interdigitated back contacts for a photoconversion efficiency Over 26%. *Nat. Energy* **2017**, *2*, 17032. [CrossRef]
3. Zhang, Y.; Liu, H. Nanowires for High-Efficiency, Low-Cost Solar Photovoltaics. *Crystals* **2019**, *9*, 87. [CrossRef]
4. Zhang, Y.; Fan, Z.; Zhang, W.; Ma, Q.; Jiang, Z.; Ma, D. High performance hybrid silicon micropillar solar cell based on light trapping characteristics of Cu nanoparticles. *AIP Adv.* **2018**, *8*, 055309. [CrossRef]
5. Salem, M.S.; Alzahrani, A.J.; Ramadan, R.A.; Alanazi, A.; Shaker, A.; Abouelatta, M.; Zekry, A. Physically based analytical model of heavily doped silicon wafers based proposed solar cell microstructure. *IEEE Access* **2020**, *8*, 138898–138906. [CrossRef]
6. Salem, M.S.; Zekry, A.; Shaker, A.; Abouelatta, M. Design and simulation of proposed low cost solar cell structures based on heavily doped silicon wafers. In Proceedings of the 2016 IEEE 43rd Photovoltaic Specialists Conference (PVSC), Portland, OR, USA, 5–10 June 2016.
7. Cui, P.; Wei, D.; Ji, J.; Huang, H.; Jia, E.; Dou, S.; Wang, T.; Wang, W.; Li, M. Planar p–n homojunction perovskite solar cells with efficiency exceeding 21.3%. *Nat. Energy* **2019**, *4*, 150–159. [CrossRef]
8. Salem, M.S.; Shaker, A.; Zekry, A.; Abouelatta, M.; Alanazi, A.; Alshammari, M.T.; Gontrand, C. Analysis of hybrid hetero-homo junction lead-free perovskite solar cells by SCAPS simulator. *Energies* **2021**, *14*, 5741. [CrossRef]
9. Ren, D.; Chen, S.; Cathelinaud, M.; Liang, G.; Ma, H.; Zhang, X. Fundamental physical characterization of Sb₂Se₃-based quasi-homojunction thin film solar cells. *ACS Appl. Mater. Interfaces* **2020**, *12*, 30572–30583. [CrossRef]
10. Shaker, A.; Salem, M.S.; Jayan, K.D. Analysis and design of pn homojunction Sb₂Se₃ solar cells by numerical simulation. *Sol. Energy* **2022**, *242*, 276–286. [CrossRef]
11. Jiang, Q.; Ni, Z.; Xu, G.; Lin, Y.; Rudd, P.N.; Xue, R.; Li, Y.; Li, Y.; Gao, Y.; Huang, J. Interfacial Molecular Doping of Metal Halide Perovskites for Highly Efficient Solar Cells. *Adv. Mater.* **2020**, *32*, e2001581. [CrossRef]
12. National Renewable Energy Laboratory. Best Research-Cell Efficiency Chart. Available online: <https://www.nrel.gov/pv/assets/pdfs/best-research-cell-efficiencies-rev220126.pdf> (accessed on 10 January 2023).
13. Zhang, F.; Zhu, K. Additive engineering for efficient and stable perovskite solar cells. *Adv. Energy Mater.* **2020**, *10*, 1902579–1902604. [CrossRef]
14. Alanazi, T.I.; Game, O.S.; Smith, J.A.; Kilbride, R.C.; Greenland, C.; Jayaprakash, R.; Georgiou, K.; Terrill, N.J.; Lidzey, D.G. Potassium iodide reduces the stability of triple-cation perovskite solar cells. *RSC Adv.* **2020**, *10*, 40341–40350. [CrossRef]

15. Abdelaziz, S.; Zekry, A.; Shaker, A.; Abouelatta, M. Investigation of lead-free $\text{MASnI}_3\text{-MASnIBr}_2$ tandem solar cell: Numerical simulation. *Opt. Mater.* **2022**, *123*, 111893. [[CrossRef](#)]
16. He, T.; Jiang, Y.; Xing, X.; Yuan, M. Structured perovskite light absorbers for efficient and stable photovoltaics. *Adv. Mater.* **2020**, *32*, 1903937–1903953. [[CrossRef](#)]
17. Singh, A.N.; Kajal, S.; Kim, J.; Jana, A.; Kim, J.Y.; Kim, K.S. Interface engineering driven stabilization of halide perovskites against moisture, heat, and light for optoelectronic applications. *Adv. Energy Mater.* **2020**, *10*, 2000768–2000807. [[CrossRef](#)]
18. Xu, J.; Saklatvala, R.; Mittal, S.; Deshmukh, S.; Procopio, A. Recent progress of potentiating immune checkpoint blockade with external stimuli—An industry perspective. *Adv. Sci.* **2020**, *7*, 1903394–1903411. [[CrossRef](#)] [[PubMed](#)]
19. Pitaro, M.; Tekelenburg, E.K.; Shao, S.; Loi, M.A. Tin halide perovskites: From fundamental properties to solar cells. *Adv. Mater.* **2022**, *34*, 2105844. [[CrossRef](#)] [[PubMed](#)]
20. Omarova, Z.; Yezhep, D.; Aldiyarov, A.; Tokmoldin, N. In silico investigation of the impact of hole-transport layers on the performance of $\text{CH}_3\text{NH}_3\text{SnI}_3$ perovskite photovoltaic cells. *Crystals* **2022**, *12*, 699. [[CrossRef](#)]
21. Liu, M.; Pasanen, H.; Ali-Loytty, H.; Hiltunen, A.; Lahtonen, K.; Qudsia, S.; Smatt, J.-H.; Valden, M.; Tkachenko, N.V.; Vivo, P. B-site co-alloying with germanium improves the efficiency and stability of all-inorganic tin-based perovskite nanocrystal solar cells. *Angew. Chem.* **2020**, *132*, 22301–22309. [[CrossRef](#)]
22. Chen, J.; Luo, Z.; Fu, Y.; Wang, X.; Czech, K.J.; Shen, S.; Guo, L.; Wright, J.C.; Pan, A.; Jin, S. Tin(IV)-tolerant vapor phase growth and photophysical properties of aligned cesium tin halide perovskite (CsSnX_3 , X = Br, I) nanowires. *ACS Energy Lett.* **2019**, *4*, 1045–1052. [[CrossRef](#)]
23. Slavney, A.H.; Hu, T.; Lindenberg, A.M.; Karunadasa, H.I. Bismuth-halide double perovskite with long carrier recombination lifetime for photovoltaic applications. *J. Am. Chem. Soc.* **2016**, *138*, 2138–2141. [[CrossRef](#)]
24. McClure, E.T.; Ball, M.R.; Windl, W.; Woodward, P.M. $\text{Cs}_2\text{AgBiX}_6$ (X = Br, Cl): New visible light absorbing, lead-free halide perovskite semiconductors. *Chem. Mater.* **2016**, *28*, 1348–1354. [[CrossRef](#)]
25. Wei, F.; Deng, Z.; Sun, S.; Zhang, F.; Evans, D.M.; Kieslich, G.; Tominaka, S.; Carpenter, M.A.; Zhang, J.; Bristowe, P.D.; et al. The synthesis and properties of a lead-free hybrid double perovskite: $(\text{CH}_3\text{NH}_3)_2\text{AgBiBr}_6$. *Chem. Mater.* **2017**, *29*, 1089–1094. [[CrossRef](#)]
26. Yang, X.; Chen, Y.; Liu, P.; Xiang, H.; Wang, W.; Ran, R.; Zhou, W.; Shao, Z. Simultaneous power conversion efficiency and stability enhancement of $\text{Cs}_2\text{AgBiBr}_6$ lead-free inorganic perovskite solar cell through adopting a multifunctional dye interlayer. *Adv. Funct. Mater.* **2020**, *30*, 2001557–2001564. [[CrossRef](#)]
27. Greul, E.; Petrus, M.L.; Binek, A.; Docampo, P.; Bein, T. Highly stable, phase pure $\text{Cs}_2\text{AgBiBr}_6$ double perovskite thin films for optoelectronic applications. *J. Mater. Chem. A* **2017**, *5*, 19972–19981. [[CrossRef](#)]
28. Gao, W.; Ran, C.; Xi, J.; Jiao, B.; Zhang, W.; Wu, M.; Hou, X.; Wu, Z. High-quality $\text{Cs}_2\text{AgBiBr}_6$ double perovskite film for lead-free inverted planar heterojunction solar cells with 2.2% efficiency. *Chem. Phys. Chem.* **2018**, *19*, 1696–1700. [[CrossRef](#)]
29. Wu, C.; Zhang, Q.; Liu, Y.; Luo, W.; Guo, X.; Huang, Z.; Ting, H.; Sun, W.; Zhong, X.; Wei, S.; et al. The dawn of lead-free perovskite solar cell: Highly stable double perovskite $\text{Cs}_2\text{AgBiBr}_6$ film. *Adv. Sci.* **2018**, *5*, 1700759–1700766. [[CrossRef](#)]
30. Wang, B.; Li, N.; Yang, L.; Dall’Agnese, C.; Jena, A.K.; Miyasaka, T.; Wang, X.F. Organic dye/ $\text{Cs}_2\text{AgBiBr}_6$ double perovskite heterojunction solar cells. *J. Am. Chem. Soc.* **2021**, *143*, 14877–14883. [[CrossRef](#)]
31. Fan, P.; Peng, H.-X.; Zheng, Z.-H.; Chen, Z.-H.; Tan, S.-J.; Chen, X.-Y.; Luo, Y.-D.; Su, Z.-H.; Luo, J.-T.; Liang, G.-X. Single-Source Vapor-Deposited $\text{Cs}_2\text{AgBiBr}_6$ Thin Films for Lead-Free Perovskite Solar Cells. *Nanomaterials* **2019**, *9*, 1760. [[CrossRef](#)]
32. Zhang, Z.; Sun, Q.; Lu, Y.; Lu, F.; Mu, X.; Wei, S.H.; Sui, M. Hydrogenated $\text{Cs}_2\text{AgBiBr}_6$ for significantly improved efficiency of lead-free inorganic double perovskite solar cell. *Nat. Commun.* **2022**, *13*, 1–12. [[CrossRef](#)]
33. Karthick, S.; Velumani, S.; Bouclé, J. Experimental and SCAPS simulated formamidinium perovskite solar cells: A comparison of device performance. *Sol. Energy* **2020**, *205*, 349–357. [[CrossRef](#)]
34. Hossain, M.K.; Rubel, M.H.K.; Toki, G.I.; Alam, I.; Rahman, M.F.; Bencherif, H. Effect of various electron and hole transport layers on the performance of CsPbI_3 -based perovskite solar cells: A numerical investigation in DFT, SCAPS-1D, and wxAMPS frameworks. *ACS Omega* **2022**, *7*, 43210–43230. [[CrossRef](#)] [[PubMed](#)]
35. Alsalmeh, A.; Altowairqi, M.F.; Alhamed, A.A.; Khan, R.A. Optimization of Photovoltaic Performance of Pb-Free Perovskite Solar Cells via Numerical Simulation. *Molecules* **2023**, *28*, 224. [[CrossRef](#)] [[PubMed](#)]
36. Alsalmeh, A.; Alsaedi, H. Twenty-Two Percent Efficient Pb-Free All-Perovskite Tandem Solar Cells Using SCAPS-1D. *Nanomaterials* **2022**, *13*, 96. [[CrossRef](#)]
37. Islam, M.T.; Jani, M.R.; Al Amin, S.M.; Sami, M.S.U.; Shorowordi, K.M.; Hossain, M.I.; Devgun, M.; Chowdhury, S.; Banerje, S.; Ahmed, S. Numerical simulation studies of a fully inorganic $\text{Cs}_2\text{AgBiBr}_6$ perovskite solar device. *Opt. Mater.* **2020**, *105*, 109957. [[CrossRef](#)]
38. Mohandes, A.; Moradi, M.; Nadgaran, H. Numerical simulation of inorganic $\text{Cs}_2\text{AgBiBr}_6$ as a lead-free perovskite using device simulation SCAPS-1D. *Opt. Quantum Electron.* **2021**, *53*, 1–22. [[CrossRef](#)]
39. Alkhamash, H.I.; Mottakin, M.; Hossen, M.M.; Akhtaruzzaman, M.; Rashid, M.J. Design and defect study of $\text{Cs}_2\text{AgBiBr}_6$ double perovskite solar cell using suitable charge transport layers. *Semicond. Sci. Technol.* **2022**, *38*, 015005. [[CrossRef](#)]
40. Burgelman, M.; Decock, K.; Niemegeers, A.; Verschraegen, J.; Degraeve, S. *SCAPS Manual*; University of Gent: Ghent, Belgium, 2014.

41. Sobayel, K.; Shahinuzzaman, M.; Amin, N.; Karim, M.R.; Dar, M.A.; Gul, R.; Alghoul, M.A.; Sopian, K.; Hasan, A.K.M.; Akhtaruzzaman, M. Efficiency enhancement of CIGS solar cell by WS₂ as window layer through numerical modelling tool. *Sol. Energy* **2020**, *207*, 479–485. [[CrossRef](#)]
42. Ahmad, O.; Rashid, A.; Ahmed, M.W.; Nasir, M.F.; Qasim, I. Performance evaluation of Au/p-CdTe/Cs₂TiI₆/n-TiO₂/ITO solar cell using SCAPS-1D. *Opt. Mater.* **2021**, *117*, 111105. [[CrossRef](#)]
43. Samiul Islam, M.; Sobayel, K.; Al-Kahtani, A.; Islam, M.A.; Muhammad, G.; Amin, N.; Shahiduzzaman, M.; Akhtaruzzaman, M. Defect Study and Modelling of SnX₃-Based Perovskite Solar Cells with SCAPS-1D. *Nanomaterials* **2021**, *11*, 1218. [[CrossRef](#)]
44. Chen, Q.; Ni, Y.; Dou, X.; Yoshinori, Y. The Effect of Energy Level of Transport Layer on the Performance of Ambient Air Prepared Perovskite Solar Cell: A SCAPS-1D Simulation Study. *Crystals* **2022**, *12*, 68. [[CrossRef](#)]
45. Moiz, S.A.; Albadwani, S.A.; Alshaikh, M.S. Towards Highly Efficient Cesium Titanium Halide Based Lead-Free Double Perovskites Solar Cell by Optimizing the Interface Layers. *Nanomaterials* **2022**, *12*, 3435. [[CrossRef](#)]
46. Zyoud, S.H.; Zyoud, A.H.; Ahmed, N.M.; Prasad, A.R.; Khan, S.N.; Abdelkader, A.F.I.; Shahwan, M. Numerical Modeling of High Conversion Efficiency FTO/ZnO/CdS/CZTS/MO Thin Film-Based Solar Cells: Using SCAPS-1D Software. *Crystals* **2021**, *11*, 1468. [[CrossRef](#)]
47. Zyoud, S.H.; Zyoud, A.H.; Ahmed, N.M.; Abdelkader, A.F.I. Numerical Modelling Analysis for Carrier Concentration Level Optimization of CdTe Heterojunction Thin Film-Based Solar Cell with Different Non-Toxic Metal Chalcogenide Buffer Layers Replacements: Using SCAPS-1D Software. *Crystals* **2021**, *11*, 1454. [[CrossRef](#)]
48. Gamal, N.; Sedky, S.H.; Shaker, A.; Fedawy, M. Design of lead-free perovskite solar cell using Zn_{1-x}Mg_xO as ETL: SCAPS device simulation. *Optik* **2021**, *242*, 167306. [[CrossRef](#)]
49. Basyoni, M.S.S.; Salah, M.M.; Mousa, M.; Shaker, A.; Zekry, A.; Abouelatta, M.; Alshammari, M.T.; Al-Dhlan, K.A.; Gontrand, C. On the Investigation of Interface Defects of Solar Cells: Lead-Based vs Lead-Free Perovskite. *IEEE Access* **2021**, *9*, 130221–130232. [[CrossRef](#)]
50. Pauwels, H.J.; Vanhoutte, G. The influence of interface state and energy barriers on the efficiency of heterojunction solar cells. *J. Phys. D Appl. Phys.* **1978**, *11*, 649–667. [[CrossRef](#)]
51. Steele, J.A.; Puech, P.; Keshavarz, M.; Yang, R.; Banerjee, S.; Debroye, E.; Kim, C.W.; Yuan, H.; Heo, N.H.; Vanacken, J.; et al. Giant electron–phonon coupling and deep conduction band resonance in metal halide double perovskite. *ACS Nano* **2018**, *12*, 8081–8090. [[CrossRef](#)]
52. Yang, X.; Xiang, H.; Huang, J.; Zhou, C.; Ran, R.; Wang, W.; Zhou, W.; Shao, Z. Thiourea with sulfur-donor as an effective additive for enhanced performance of lead-free double perovskite photovoltaic cells. *J. Colloid Interface Sci.* **2022**, *628*, 476–485. [[CrossRef](#)]
53. Kumar, A.; Thakur, A.D. Role of contact work function, back surface field, and conduction band offset in Cu₂ZnSnS₄ solar cell. *Jpn. J. Appl. Phys.* **2018**, *57*, 08RC05. [[CrossRef](#)]
54. Minemoto, T.; Murata, M. Theoretical analysis on effect of band offsets in perovskite solar cells. *Sol. Energy Mater. Sol. Cells* **2015**, *133*, 8–14. [[CrossRef](#)]
55. Smith, J.A.; Game, O.S.; Bishop, J.E.; Spooner, E.L.; Kilbride, R.C.; Greenland, C.; Jayaprakash, R.; Alanazi, T.I.; Cassella, E.J.; Tejada, A.; et al. Rapid scalable processing of tin oxide transport layers for perovskite solar cells. *ACS Appl. Energy Mater.* **2020**, *3*, 5552–5562. [[CrossRef](#)] [[PubMed](#)]
56. Solís-Vivanco, J.F.; Aruna-Devi, R.; Arenas-Arrocena, M.C.; Sosa-Domínguez, A.; De Moure-Flores, F.J.; Santos-Cruz, J. Double ETL in ITO-free poly-3-hexylthiophene-based organic solar cells. In Proceedings of the 2021 18th International Conference on Electrical Engineering, Computing Science and Automatic Control (CCE), Mexico City, Mexico, 10–12 November 2021; pp. 1–5.
57. Li, C.; Xu, H.; Zhi, C.; Wan, Z.; Li, Z. TiO₂/SnO₂ electron transport double layers with ultrathin SnO₂ for efficient planar perovskite solar cells. *Chin. Phys. B* **2022**, *31*, 118802. [[CrossRef](#)]
58. Huang, W.; Zhang, R.; Xia, X.; Steichen, P.; Liu, N.; Yang, J.; Chu, L.; Li, X.A. Room temperature processed double electron transport layers for efficient perovskite solar cells. *Nanomaterials* **2021**, *11*, 329. [[CrossRef](#)]
59. Zhao, Y.; Li, C.; Niu, J.; Zhi, Z.; Chen, G.; Gong, J.; Li, J.; Xiao, X. Zinc-based electron transport materials for over 9.6%-efficient S-rich Sb₂(S, Se)₃ solar cells. *J. Mater. Chem. A* **2021**, *9*, 12644–12651. [[CrossRef](#)]
60. Gharibshahian, I.; Orouji, A.; Sharbati, S. Efficient Sb₂(S,Se)₃/Zn(O,S) solar cells with high open-circuit voltage by controlling sulfur content in the absorber-buffer layers. *Sol. Energy* **2021**, *227*, 606–615. [[CrossRef](#)]
61. Rühle, S. Tabulated values of the Shockley–Queisser limit for single junction solar cells. *Sol. Energy* **2016**, *130*, 139–147. [[CrossRef](#)]

Disclaimer/Publisher’s Note: The statements, opinions and data contained in all publications are solely those of the individual author(s) and contributor(s) and not of MDPI and/or the editor(s). MDPI and/or the editor(s) disclaim responsibility for any injury to people or property resulting from any ideas, methods, instructions or products referred to in the content.